Ab initio based empirical potential used to study the mechanical properties of molybdenum

Hyoungki Park,[1,*] Michael R. Fellinger,[1] Thomas J. Lenosky,[2] William W. Tipton,[3] Dallas R. Trinkle,[4] Sven P. Rudin,[5] Christopher Woodward,[6] John W. Wilkins,[1] and Richard G. Hennig[1,3]

[1]*Department of Physics, The Ohio State University, Columbus, Ohio 43210, USA*
[2]*1974 Kirby Way, San Jose, California 95124-1324, USA*
[3]*Department of Materials Science and Engineering, Cornell University, Ithaca, New York 14853-1501, USA*
[4]*Department of Material Science and Engineering, University of Illinois at Urbana-Champaign, Urbana, Illinois 61801, USA*
[5]*Los Alamos National Laboratory, Los Alamos, New Mexico 87545, USA*
[6]*Materials and Manufacturing Directorate, Air Force Research Laboratory, Wright-Patterson Air Force Base, Dayton, Ohio 45433, USA*

Density-functional theory energies, forces, and elastic constants determine the parametrization of an empirical, modified embedded-atom method potential for molybdenum. The accuracy and transferability of the potential are verified by comparison to experimental and density-functional data for point defects, phonons, thermal expansion, surface and stacking fault energies, and ideal shear strength. Searching the energy landscape predicted by the potential using a genetic algorithm verifies that it reproduces not only the correct bcc ground state of molybdenum but also all low-energy metastable phases. The potential is also applicable to the study of plastic deformation and used to compute energies, core structures, and Peierls stresses of screw and edge dislocations.

PACS number(s): 62.20.−x, 34.20.Cf, 63.20.−e, 61.72.J−

I. INTRODUCTION

Molybdenum's high strength and high-temperature stability make this refractory metal very attractive for use in advanced process technologies. The motion of dislocations is generally accepted to be responsible for the complex deformation behavior of this transition metal.[1–8] In recent years progress has been made on the description of the properties of screw dislocations using density-functional theory (DFT), tight-binding calculations, and empirical potentials.[9–19] However, DFT and tight-binding techniques are limited to small system sizes, which is problematic due to the long-range strain field of dislocations, and current empirical potentials lack the required accuracy for the description of the dislocation structure. Simulations of dislocation motion and interactions require efficient interatomic potentials which accurately describe the dislocation energies, core structures, and motion.

In this work we develop an empirical potential for Mo which predicts the ideal shear strength, generalized stacking fault energies, energies of dislocations, and the Peierls stress and core structure of the $\langle 111 \rangle /2$ screw dislocation. The potential form is given by the modified embedded-atom method (MEAM) and the potential parameters are optimized using *ab initio* energies, lattice parameters, forces, and elastic constants. Section II describes the calculations for the DFT database, the functional form of the MEAM potential, and the optimization of the potential parameters to the DFT database. The accuracy of the potential for structural, elastic, and defect properties is verified in Sec. III by comparison to DFT results and experiments. A genetic algorithm search of the energy landscape of the MEAM potential confirms that the potential reproduces the correct bcc ground state and predicts several low-energy metastable structures whose energies agree well with DFT results. Results of the MEAM potential for formation energies of point defects, phonon dispersion, thermal expansion, surface energies, ideal shear strength, and generalized stacking faults for the MEAM potential closely match DFT results and available experimental data. In Sec. IV we apply the potential to determine energies

and Peierls stresses of the screw and edge dislocation in bcc Mo. The results show that the MEAM potential accurately describes the structural and mechanical properties of Mo and should be applicable to simulate the motion of dislocations and the plastic deformation of Mo.

II. OPTIMIZATION OF THE EMPIRICAL POTENTIAL TO DENSITY-FUNCTIONAL THEORY DATABASE

We develop an empirical potential to efficiently describe the interactions between Mo atoms and to enable large-scale molecular-dynamics (MD) simulations. The modified embedded-atom method provides the form of the potential[20–22] with potential parameters optimized to a database of DFT calculations. The optimization of the model proceeds iteratively. Systematically adding DFT results to the fitting database improves the accuracy and extends the applicability of the model. This enables the development of a potential that accurately reproduces the structural and mechanical properties of Mo relevant for the description of its mechanical behavior. Available experimental data and DFT calculations confirm the accuracy of the resulting Mo MEAM potential.

A. Density-functional calculations

The DFT calculations are performed with VASP,[23,24] which is a density-functional code using a plane-wave basis and the projector-augmented wave method.[25,26] In addition to the $4s$ and $5d$ valence states, the $4p$ semicore states are treated explicitly to accurately describe interactions at small interatomic separations. The Perdew-Burke-Ernzerhof (PBE) generalized-gradient approximation (GGA) for the exchange-correlation functional is used for the exchange-correlation energy.[27] A plane-wave energy cutoff of 600 eV ensures energy convergence to 0.1 meV/atom. We keep the density of the k-point mesh equivalent to a $31 \times 31 \times 31$ mesh for the bcc primitive cell for all DFT calculations.

B. Modified embedded-atom potential

The MEAM formalism was originally developed by Baskes[20] as an extension of the embedded-atom method and incorporates a series of four angular dependent terms with s, p, d, and f character to model the effects of bond bending. The original MEAM potential has been applied to a variety of systems ranging from the semiconductors Si[20,28] and Ge[29] to bcc, fcc, and hcp metals[30–32] and to several binary-alloy systems.[29,33]

Lenosky *et al.* modified the original MEAM potential by using cubic splines for the functional form.[21] This removes the constraint of fixed angular character and allows for additional flexibility of the potential. Furthermore, the use of splines reduces the cost of evaluation over the original functional form, providing increased computational efficiency. The spline-based MEAM was successfully applied to study defects in Si[21,34–40] and martensitic phase transformations in Ti.[22] This success of the spline-based MEAM, its improved flexibility, and its higher computational efficiency motivate our use of this functional form here. The MEAM potential is implemented into two freely available large-scale parallel molecular-dynamics codes.[41,42]

The MEAM potential[21] used in this work separates the energy into two parts, the pair energy and the embedding energy:

$$E = \frac{1}{2} \sum_{ij} \phi(r_{ij}) + \sum_{i} U(n_i), \quad (1)$$

with the density at atom i

$$n_i = \sum_{j} \rho(r_{ij}) + \frac{1}{2} \sum_{jk} f(r_{ij}) f(r_{ik}) g[\cos(\theta_{jik})], \quad (2)$$

where θ_{jik} is the angle between atoms j, i, and k, centered on atom i, and r_{ij} is the separation between atoms i and j. The functional form contains as special cases the Stillinger-Weber[43] method [$U(x) = x$ and $\rho = 0$] and the embedded-atom method (EAM) ($f = 0$ or $g = 0$) potentials. The five functions $\phi(r)$, $U(\rho)$, $\rho(r)$, $f(r)$, and $g[\cos(\theta)]$ are represented by cubic splines.[44] This allows for the necessary flexibility to accurately describe complex systems and provides the computational efficiency required for large-scale molecular-dynamics simulations.

Splines are optimized from parameters of a good potential for Nb, another refractory body-centered-cubic metal. This optimization uses the Powell least-squares local optimizer.[45] The niobium model parameters are obtained by first doing a set of 62 global optimizations, followed by a set of 22 local optimizations, with varying weights, cutoffs, and control parameters. For the global optimizer, we use a least-squares scheme based on the parallel tempering method.[46–48] Table I lists the resulting spline parameters of the Mo MEAM potential. In the following section we compare the fit results and prediction of the MEAM potential with DFT and experimental data to establish the accuracy and transferability of the potential.

The DFT database for the fitting of the potential parameters consists of the formation energy of the vacancy using a $54 - 1$

TABLE I. Parameters specifying the five cubic splines that comprise the Mo MEAM potential. The first part of the table lists the number of knots N for each spline and the range of the spline variables $t_{\min}$ and $t_{\max}$. The middle part of the table gives the values at equally spaced spline knots defined by $t_i = t_{\min} + i(t_{\max} - t_{\min})/N$ where N is the number of spline knots. Finally, the derivatives of the splines at their end points are listed in the last part of the table.

	t	$t_{\min}$	$t_{\max}$	N	
ϕ	r[Å]	2.011871291713	5.900000000000	13	
ρ	r[Å]	2.011871291713	5.100000000000	12	
f	r[Å]	2.011871291713	5.100000000000	12	
U	ρ_{tot}	−95.855074371885	−32.122459255304	3	
g	$\cos(\theta)$	−1.000000000000	0.999879036544	8	
i	$\phi(r_i)$ (eV)	$\rho(r_i)$	$f(r_i)$	$U(\rho_i)$ (eV)	$g(x_i)$
0	4.632438733669	−26.494449971737	3.388227678515	−1.501526682314	−0.129869313833
1	1.752489147287	−17.205090985947	2.420736204325	−0.356089776173	0.379321594386
2	0.438243695515	−8.514689239696	1.383682254891	2.322962191866	−0.005269150527
3	−0.015797259725	−4.576484741434	0.418171427726		−0.337540972877
4	−0.068300083022	−3.265714893932	−0.366113294172		−0.454061549494
5	−0.059263239247	−2.480415753371	−0.554323601336		−0.200674288922
6	−0.086981977667	−1.297204680368	−0.227358024429		−0.942045838810
7	−0.058881015541	−0.123839105776	−0.050257216206		−6.817412868037
8	−0.031430767187	0.000631923191	0.026183906447		
9	−0.019141100155	−0.227021672597	0.000384787223		
10	−0.007063383114	−0.081165548268	−0.000619452297		
11	−0.001171831136	0.000000000000	0.000000000000		
12	0.000000000000				
i	$\phi'(r)$ (eV/Å)	$\rho'(r)$ (Å^{-1})	$f'(r)$ (Å^{-1})	$U'(\rho)$ (eV)	$g'(x)$
0	−11.529904170892	0.000000000000	0.000000000000	0.022915774551	2.614296175470
N	0.000000000000	0.000000000000	0.000000000000	0.130788918963	−24.328955341990

atom simulation cell, energies as a function of lattice constant from $a = 2.95$ to 3.35 Å, elastic constants, and forces, all computed for the bcc phase. For DFT forces, three atomic configurations are generated from snapshots of *ab initio* molecular-dynamics (MD) simulations with simulation cells containing 125 atoms at 1270 K (bcc), 2320 K (bcc), and 5270 K (liquid). For the force data, the relative rms deviation of the MEAM force magnitudes from the DFT values is 11%, and the average angular deviation of the MEAM force directions from the DFT force directions is 6.4°. Weighting the averages by the scaled DFT force magnitude decreases these values further to 9% and 5.5°, respectively.

III. ACCURACY OF THE MEAM POTENTIAL

We test the quality of the potential by comparing a wide variety of computed properties to DFT calculations and experimental data. We implemented the MEAM potential into the LAMMPS[52] code, which was used to perform all the empirical potential simulations. Predictions of the potential confirm its accuracy and transferability.

A. Structural and elastic properties

Table II compares the MEAM cohesive energies, lattice parameters, and elastic constants with the DFT values for

TABLE II. The MEAM values for the cohesive energy, lattice parameter, bulk modulus, and elastic constants of bcc Mo compared to DFT and experiment. The energies and lattice parameters of the fcc, hcp, β-W, β-Ta, ω-Ti, monoclinic C2/m, Fddd, and Pmma structures are compared to DFT results. The energies are relative to the energy of the bcc structure.

	MEAM[a]	GGA-PBE[a]	Exp.
E_{coh} (eV/atom)	6.82	6.25	6.82[b]
a (Å)	3.167	3.169	3.147[c]
B (G Pa)	253	263	270[d]
C_{11} (G Pa)	441	462	479[d]
C_{12} (G Pa)	158	163	165[d]
C_{44} (G Pa)	96	102	108[d]
$\Delta E_{C2/m-bcc}$ (meV/atom)	198	164	
$\Delta E_{Pmma-bcc}$ (meV/atom)	242	221	
$\Delta E_{\beta W-bcc}$ (meV/atom)	266	96	
$a_{\beta W}$ (Å)	5.026	5.058	
$\Delta E_{Fddd-bcc}$ (meV/atom)	269	233	
$\Delta E_{\beta Ta-bcc}$ (meV/atom)	280	168	
$a_{\beta Ta}$ (Å)	9.719	9.752	
$c_{\beta Ta}$ (Å)	5.048	5.113	
$\Delta E_{\omega Ti-bcc}$ (meV/atom)	332	404	
$a_{\omega Ti}$ (Å)	4.616	4.681	
$c_{\omega Ti}$ (Å)	2.595	2.572	
$\Delta E_{fcc-bcc}$ (meV/atom)	391	418	
a_{fcc} (Å)	3.931	4.013	
$\Delta E_{hcp-bcc}$ (meV/atom)	415	433	
a_{hcp} (Å)	2.743	2.765	
c_{hcp} (Å)	4.692	4.905	

[a]This work.

[b]Experimental data from Brewer.[49]

[c]Experimental data from Pearson.[50]

[d]Experimental data from Simmons and Wang.[51] The bulk modulus is obtained from C_{11} and C_{12}: $B = (C_{11} + 2C_{12})/3$.

the experimentally observed bcc phase and the fcc, hcp, β-W, β-Ta, ω-Ti, monoclinic C2/m, orthorhombic Fddd, and orthorhombic Pmma structures. The experimental cohesive energy of the bcc structure is 6.82 eV, and DFT produces a cohesive energy 8% lower than the experimental value.[53] The MEAM is fitted to the experimental cohesive energy. The fitted lattice parameter of the MEAM potential, 3.167 Å, agrees closely with the DFT value of 3.169 Å.

The bcc crystal structure is stable against the fcc and hcp structures. DFT predicts that the energies of fcc and hcp Mo are 418 and 433 meV/atom larger than the bcc value, respectively. The MEAM potential predicts similar values of 391 and 415 meV/atom. Our MEAM potential predicts a c/a value of 1.71 for the hcp structure, closely matching the DFT value of 1.77. In addition, energies with the MEAM potential for the β-W, β-Ta, and ω-Ti structures are higher than the bcc energy. The lattice parameters of all the structures are reproduced reasonably well, with the largest error being for the hcp c value. No DFT data for the fcc, hcp, β-W, β-Ta, and ω-Ti structures are included in the fitting database.

The calculated DFT bulk modulus and elastic constants match experimental values within 5% error. The fitted MEAM values agree with the DFT values within 6%. The bulk modulus is determined by calculating the energy of bcc Mo for the volume range $0.90V_0 < V < 1.10V_0$, where V_0 is the equilibrium volume, and fitting the third-order Birch-Murnaghan equation of state[54,55] to the results. The elastic constants are determined by applying several strains ranging from -1 to $+1\%$. The DFT and MEAM elastic constants are evaluated at the respective computed equilibrium volume of each method.

B. Potential-energy landscape

The GASP code[56,57] (genetic algorithm for structure prediction) was used to search for low-energy structures using the MEAM potential. This algorithm begins by randomly generating a population of structures. These structures are relaxed using LAMMPS and ranked according to their energies. The better (lower-energy) structures are more likely to be used to create a subsequent generation of candidate solutions. This reproduction occurs via several operators designed to pass down essential properties of parent structures to the children. In this way, the population of structures improves over time, and the algorithm should find the ground state and many other low-energy structures.

This search allows us to check that our potential reproduces the known true ground state of molybdenum (a bcc crystal) and to identify low-energy metastable phases. Unit cells of up to 40 atoms were considered, and the search ran for 100 generations with 100 distinct candidate structures in each generation. The bcc and various defect and metastable structures were encountered by the algorithm many times. The bcc crystal is the lowest-energy structure found.

In addition to many structures representing defects in a bcc cell, several notable metastable crystal structures were identified by the genetic algorithm. The lowest energy of these is a five-atom monoclinic C2/m structure. The formation energy per atom compared to bcc according to MEAM (DFT) is $+198$ meV/atom ($+164$ meV/atom). Next, we find a

TABLE III. Comparison of defect formation energies in units of eV in bcc Mo between DFT calculations and empirical potentials. For the vacancy, migration energies are shown as well. Only the vacancy formation energy is included in the fitting database.

Defect	MEAM[a]	DFT[a]	DFT[b]	DFT[c]	MGPT[d]	F-S[e]
Vacancy	2.96	2.79	2.96		2.9	2.5
Vac. migration	1.64	1.22	1.28		1.6	1.3
Octahedral	8.07	9.05	9.07	8.86	17.5	7.6
Tetrahedral	8.20	8.47	8.40	8.20	14.9	7.6
$\langle 001 \rangle$ dumbbell	7.82	8.90	9.00	8.77	16.3	7.2
$\langle 011 \rangle$ dumbbell	7.68	7.66	7.58	7.51	10.9	7.0
$\langle 111 \rangle$ dumbbell	7.66	7.52	7.42	7.34	14.2	7.3
Crowdion	7.64	7.52	7.42	7.34	13.9	7.2

[a]This work.
[b]DFT results of Nguyen-Manh *et al.*[58]
[c]DFT results of Han *et al.*[59]
[d]MGPT results of Xu and Moriarty.[9]
[e]F-S results of Harder and Bacon.[60]

four-atom structure with space group 51 (Pmma) and with a MEAM (DFT) energy relative to bcc of $+242$ meV/atom ($+221$ meV/atom). The A15 (β-W) phase is $+266$ meV/atom ($+96$ meV/atom) above bcc, and a two-atom structure with space group 70 (Fddd) has energy $+269$ meV/atom ($+233$ meV/atom) above bcc. Table II includes a summary of these structures, and Fig. 2(a) shows energy-volume curves of three metastable phases and bcc for the DFT calculations and the MEAM potential.

We found no other crystal structures within 270 meV of the ground state. This result provides very strong indication that this potential has the correct ground state and that no other crystal phase should occur in any MD simulations for pressure and temperature ranges as described in this paper. The potential's reproduction of the correct ground state and accurate description of the low-lying metastable structures indicate that the potential captures many of the important properties of the *ab initio* potential-energy landscape.

C. Point defects

Vacancies have important implications for many material processes including dislocation motion and creep. On the other hand, the equilibrium concentration of self-interstitial atoms in metals is much smaller than the concentration of vacancies. Accordingly, we include the energy and the relaxed atomic configuration of the vacancy in our fitting database, but not from interstitial configurations. We use 251-atom and 6750-atom simulation cells for our DFT and MEAM calculations, respectively, to determine the formation and the migration energies of the vacancy and the formation energies of six self-interstitial configurations.

Table III lists our DFT and MEAM results, along with other published DFT,[58,59] model generalized pseudopotential theory (MGPT) potential,[9] and Finnis-Sinclair potential[60] results. Vacancy formation energies from our MEAM potential and DFT calculations closely agree with the previous DFT results and are within the range of experimental values.[61] The MEAM potential reproduces the high formation energies of all the interstitial structures reasonably well with the largest
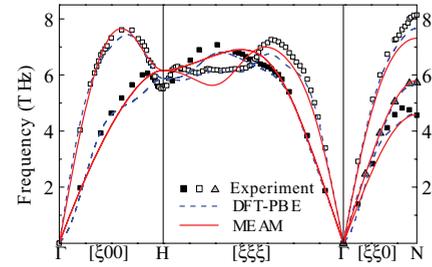
FIG. 1. (Color online) Phonon-dispersion curves for the empirical MEAM potential compared to experiment[62] and our DFT calculations. The MEAM and DFT results match experiment well over the three high-symmetry directions shown.

error for octahedral and $\langle 001 \rangle$ split dumbbell interstitials. For the crowdion, $\langle 111 \rangle$ split, and $\langle 011 \rangle$ split interstitials, the differences between our MEAM and DFT values are less than 2%.

D. Phonon dispersion, equation of state, thermal expansion, and melting temperature

We compute the phonon spectra along high-symmetry directions in the Brillouin zone and calculate the thermodynamic behavior of the potential. These calculations demonstrate the applicability of the potential over a large range of temperatures and pressures.

Figure 1 compares the computed phonon spectra along the [$\xi 00$], [$\xi \xi \xi$], and [$\xi \xi 0$] directions to experimental data[62] and our DFT calculations. The results of our MEAM potential closely match the experimental data and our DFT calculation over much of the Brillouin zone, reflecting the accuracy of the force matching and the elastic constants. Our DFT calculation is carried out with 512 atoms (an $8 \times 8 \times 8$ supercell). Since we employ the small-displacement method,[65] using this large supercell greatly improves the agreement of our DFT calculations with experiment over previously published results.[19]

Figure 2(a) shows the result of the energy fit at different volumes for the bcc phase and calculated energy-volume curves for three lowest metastable phases described in Sec. III B. The DFT and MEAM energies of the bcc phases are in excellent agreement for the fitted range of -19 to $+18\%$ V_0. Energy-volume curves for three lowest metastable phases are computed for the range of -15 to $+15\%$ V_0. The agreement between DFT and MEAM energy-volume curves for these metastable phases is not satisfactory, and it is anticipated considering that only bcc phase data are included in the fitting database. However, since the MEAM potential accurately reproduces the energy-volume curve for the bcc phase and has bcc as the most stable phase for the range of volumes we studied, we believe that the MEAM potential is sufficient to study mechanical properties of bcc Mo. Figure 2(b) shows the pressure variation of the MEAM potential versus the relative volume V/V_0, where V_0 is the zero-pressure volume, from static calculations and from *N*-*P*-*T* MD simulations at 293 K. We compare the results to data from shock experiments[63] and our zero-temperature DFT calculations. For pressures up to 30 G Pa, the agreement of the MEAM potential with DFT and experiment is excellent with pressure deviations of less than 1
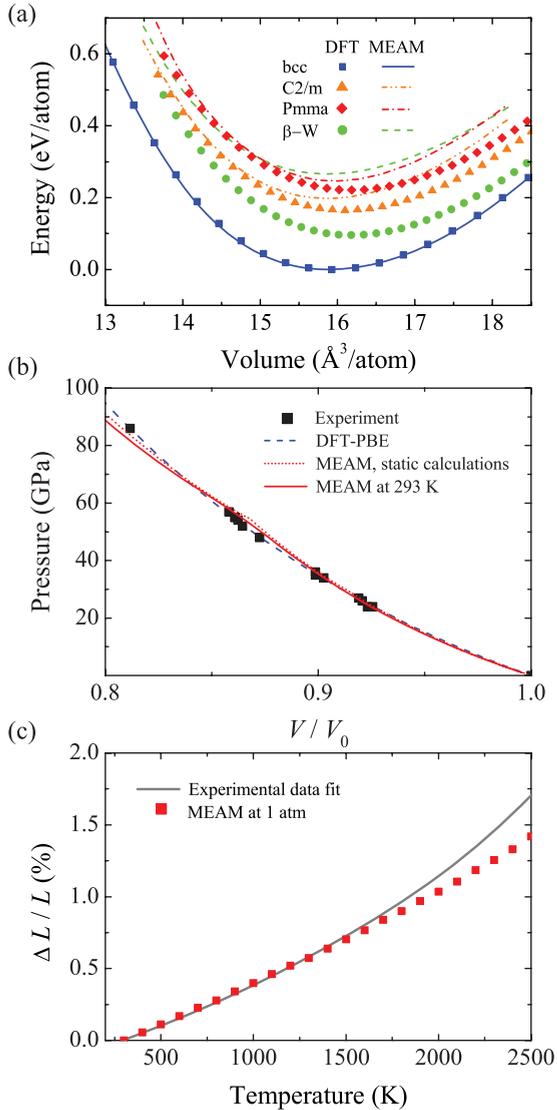
FIG. 2. (Color online) (a) Fitted energies of bcc Mo as a function of volume and calculated energy-volume curves for the three lowest metastable phases. (b) Pressure vs volume curve. The experimental data are from shock experiments.[63] For pressures up to 80 G Pa, our MEAM potential agrees well with experimental data and our DFT calculations. (c) Thermal-expansion curve. The thermal expansion of our MEAM potential agrees closely with experiments[64] up to 2000 K.

G Pa. There is a kink around $V/V_0 = 0.87$ in static calculation results for our MEAM potential. We find that the kink is caused by the discontinuity of curvature in the energy-volume curve of the MEAM potential, at $V = 13.8$ Å^3/atom in Fig. 2(a). However, this second-order derivative discontinuity is hardly noticeable in Fig. 2(a) and causes less than 5-G Pa deviations of our MEAM results from DFT and experiment data in Fig. 2(b). The kink is less pronounced in results from simulations at 293 K. Constant-*N-P-T* MD simulations of 2000 atoms at $T = 293$ K are performed with a 2-G Pa pressure step to yield the pressure-volume curve. Each MD simulation runs for 50 000 steps with a 1-fs time step, and we determine the volume for each pressure by averaging over the last 5000 simulation steps.

Figure 2(c) shows the thermal expansion of the MEAM potential for temperatures up to 2000 K. Our results closely follow the experimental data,[64] indicating that the potential accurately interpolates to temperatures not included in the fit. Constant-*N-P-T* MD simulations of 2000 atoms at $P = 1$ atm yield the thermal-expansion curve. Each MD simulation runs for 50 000 steps with a 1-fs time step and the lattice constant for each temperature is determined by averaging over the last 5000 simulation steps.

Two-phase melting simulations, in which the simulation cells contain solid and liquid in contact with each other, produce reliable melting temperatures. We follow the approach of Belonoshko *et al.*,[68] in which constant-*N-P-T* MD simulations determine the melting temperature. Simulations with about 16 500 atoms run for 500 000 steps with a 1-fs time step. We check the coexistence of the phases at the melting temperature using at least five independent simulations. We find that 130 000-atom simulations produce the same melting temperatures as 16 500-atom simulations. The simulated melting temperature of the bcc phase at $P = 1$ atm is $T_m = 3220 \pm 10$ K. Like our previous MEAM potentials for Si (Ref. 21) and Ti (Ref. 22), and the EAM potential for Nb (Ref. 69), the simulated melting temperature for our Mo MEAM is in good agreement with the experimentally measured value. It is about 10% higher than the experimental melting temperature of 2900 K.[70]

E. Surface energies

Surface properties serve as a good test bed for the transferability of our potential to configurations with low coordination numbers, since no surface data are used in constructing the potential. Table IV lists the relaxed surface energies and the surface relaxations for the {110}, {100}, and {111} surfaces. We compare the surface energies to our DFT results and published MEAM calculations.[67] The experimental value of 180 meV/Å^2 is an extrapolated value for polycrystalline Mo based on the temperature dependency of surface energies.[66]

The {100} surfaces of Mo undergo a reconstruction near room temperature.[71] However, the simply relaxed (1×1) surface structure is at least metastable against any known reconstruction.[72] All the values in Table IV are for unreconstructed surfaces. The overall agreement of the MEAM surface energies with the DFT values is quite good, considering the fact that free surfaces are not used to optimize the potential. The

TABLE IV. Low-index surface energies of bcc Mo in meV/Å^2 and the relative percent change in the interplanar spacing between the first and the second layers upon relaxation in parentheses. Our MEAM results closely match our DFT values, even though no surface data are used to construct the potential. The experimental value, 180 meV/Å^2, is for a polycrystalline solid and extrapolated from high-temperature experimental data to room temperature.[66]

Surface	MEAM[a]	GGA-PBE[a]	MEAM[b]
$E_{\text{surf}}^{\{110\}}$	164 (−4.5%)	174 (−4.4%)	180 (−3.3%)
$E_{\text{surf}}^{\{100\}}$	180 (−11.0%)	200 (−12.3%)	195 (−3.3%)
$E_{\text{surf}}^{\{111\}}$	201 (−23.6%)	186 (−20.8%)	211 (−14.0%)

[a]This work.
[b]2NN MEAM results of Lee *et al.*[67]
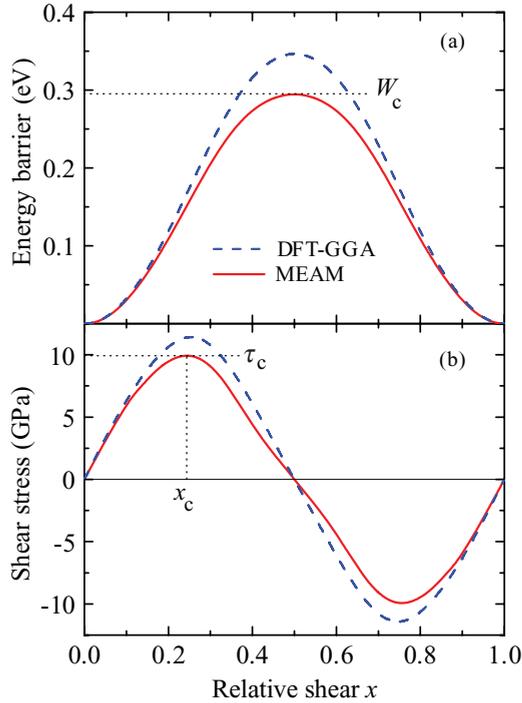
FIG. 3. (Color online) Ideal shear strength of bcc Mo calculated with the MEAM potential and DFT: (a) energy barrier $W(x)$ and (b) shear stress $\tau(x)$.

deviations are within 10%, and the {110} is the lowest-energy surface for DFT and MEAM potentials. Our MEAM values for the percent changes in the relaxed spacing between the first and second surface layers agree very closely with our DFT calculations.

The MEAM calculations use slab-geometry simulation cells with two free surfaces and periodic boundary conditions in the directions perpendicular to the surface normals. Our MEAM calculations use 300-layer slabs. The DFT calculations use a 48-layer slab for the {100} surface and 24-layer slabs for the {110} and {111} surfaces. A vacuum region 15 Å thick separates the periodic surface images for the DFT calculations.

F. Ideal shear strength

Figure 3 compares the ideal shear strength of the MEAM potential with our DFT results, without tensile relaxation. The ideal shear strength is defined as the maximum stress, τ_c, along the twinning path transforming the directions [$\bar{1}11$] and [$1\bar{1}1$] into $1/3[\bar{2}12]$ and $1/3[1\bar{2}2]$, respectively.[9,73] The ideal shear stress occurs at the critical shear x_c that separates regimes of elastic and plastic deformation of the crystal. We compute energies of 1000 deformed structures along the twinning path for both our MEAM and DFT and calculate the barrier height W_c. Numerical differentiation of these energies with respect to shear generates shear stresses and determines the critical stress τ_c and the critical shear x_c. Table V compares our MEAM results to our DFT results, published results from the full potential linear muffin-tin orbital (FPLMTO) using the local-density approximation functional,[73] and MGPT calculations.[9] Results of our MEAM potential agree with our DFT values within 15% for both energy and stress. No

TABLE V. Calculated ideal shear strength for Mo. Barrier height W_c is in eV and critical stress is in G Pa.

	MEAM[a]	GGA-PBE[a]	FPLMTO[b]	MGPT[c]
W_c	0.30	0.35	0.42	0.47
x_c	0.24	0.25	0.26	0.27
τ_c	9.9	11.4	19	23.7

[a]This work.
[b]Non-self-consistent results of Paxton *et al.*[73]
[c]MGPT results of Xu and Moriarty.[9]

deformed structures along the twinning path are included in our fitting database.

G. {110} and {112} γ surfaces

The energies of the generalized stacking faults, or γ surfaces,[74] are related to the dislocation core structure and the Peierls stress. A generalized stacking fault is obtained by cutting a perfect crystal across a single plane into two parts and displacing the parts relative to each other by an in-plane vector **d**. The excess energy $\gamma(\mathbf{d})$ generates a surface which represents the energies of generalized stacking faults. The restoring stress acting across the plane has the same interpretation as the restoring stress in the Peierls-Nabarro dislocation model.

The γ surfaces provide an ideal test of the accuracy of the MEAM potential under changes in bond direction and coordination number. We use our MEAM potential to compute unrelaxed and relaxed (112) and (011) γ surfaces in the [$\bar{1}\bar{1}1$] direction. In the relaxed MEAM calculations, the atoms are allowed to move only in the direction perpendicular to the fault plane. Figure 4 compares the energies of the γ surfaces of MEAM with the unrelaxed DFT results. Our MEAM results
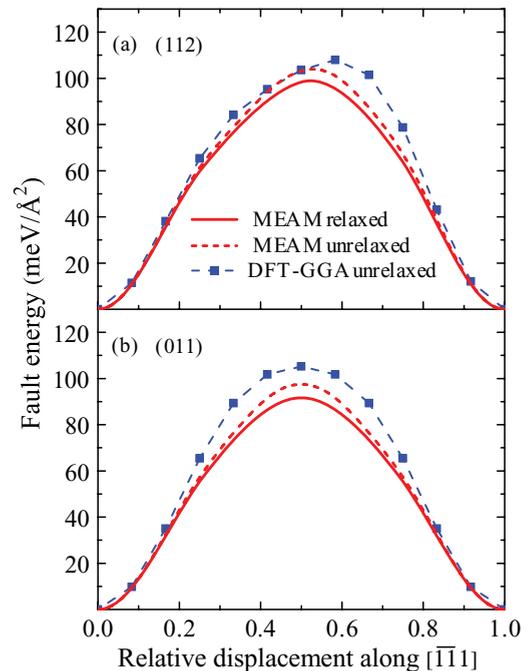
FIG. 4. (Color online) Cross sections of the (112) and (011) γ surfaces calculated with the MEAM potential and by DFT.

show slightly less asymmetry for the (112) γ surface than DFT, but the overall agreement is very good considering no stacking fault data are included in the fitting database.

For γ-surface calculations of our MEAM potential, 60 000-atom cells are used. $[1\bar{1}0]$, $[11\bar{1}]$, and $[112]$ are chosen along the x, y, and z axes, respectively, for the $\{211\}$ γ line calculation, and $[112]$, $[11\bar{1}]$, and $[1\bar{1}0]$ are used for the $\{110\}$. The DFT calculations use supercells with 24 layers for the $\{211\}$ and 12 layers for the $\{110\}$ fault plane. Energies are calculated as the top half of the block in the z axis is displaced along $[11\bar{1}]$. To apply the periodic boundary conditions in all three dimensions, the lattice vector of the supercell in the z axis is inclined by the displacement vector of the top half block. For the relaxed line, the atomic positions are relaxed only in the direction perpendicular to the cut plane, i.e., along the z axis. Computational cells with 24 atoms are used for DFT calculations.

IV. APPLICATION TO DISLOCATIONS

The low-temperature plasticity of bcc metals is dominated by the properties of $\langle 111\rangle/2$ screw dislocations. In contrast to the highly mobile edge dislocation, the screw dislocation motion is constrained by the large primary Peierls barrier for double kink nucleation. In order to model the screw dislocation core, a cell is constructed using the lattice directions: $\langle 1\bar{2}1\rangle$, $\langle\bar{1}01\rangle$, and $\langle 111\rangle$. In this dislocation coordinate system the third lattice vector is chosen parallel to the dislocation line direction and the Burgers vector, consistent with the definition of a screw dislocation [see Fig. 6(a)]. Periodic boundary conditions are applied along $\langle 111\rangle$ using a periodic unit of $a/2\langle 111\rangle$. The first two lattice vectors are then used to define a large, 91 160-atom cell and the atomic positions are displaced according to the anisotropic elastic strain field of an $a/2\langle 111\rangle$ screw dislocation. In order to relax the dislocation core, the regions near the surface of the cell are held fixed while the forces for an inner region of 76 610 atoms are optimized based on the interatomic forces. This approach allows the long-range anisotropic solution to provide the correct boundary conditions for the cell interior. The detailed description of the simulation setup can be found in our previous work on an EAM potential for niobium.[69] For the $\frac{1}{2}\langle 111\rangle\{112\}$ edge dislocation we use a similar fixed-boundary condition and a total of 148 368 atoms with 137 928 atoms in the inner relaxed region.

In general elasticity theory of dislocation, the energy of a dislocation per unit length, E, comes from the elastic part that is contained in the elastically strained bonds outside the radius r_0 and from the energy stored in the core, which is not amenable to elasticity theory and cannot be defined uniquely. For the screw dislocation,

$$E^{\mathrm{s}} = E^{\mathrm{s}}_{\mathrm{core}} + \frac{Kb^2}{4\pi}\ln\left(\frac{r}{r_0}\right), \qquad (3)$$

and, for the edge dislocation,

$$E^{\mathrm{e}} = E^{\mathrm{e}}_{\mathrm{core}} + \frac{Kb^2}{4\pi(1-\nu)}\ln\left(\frac{r}{r_0}\right), \qquad (4)$$

where r_0 is the core radius of the dislocation and r is the external radius of the elastic cylinder containing the
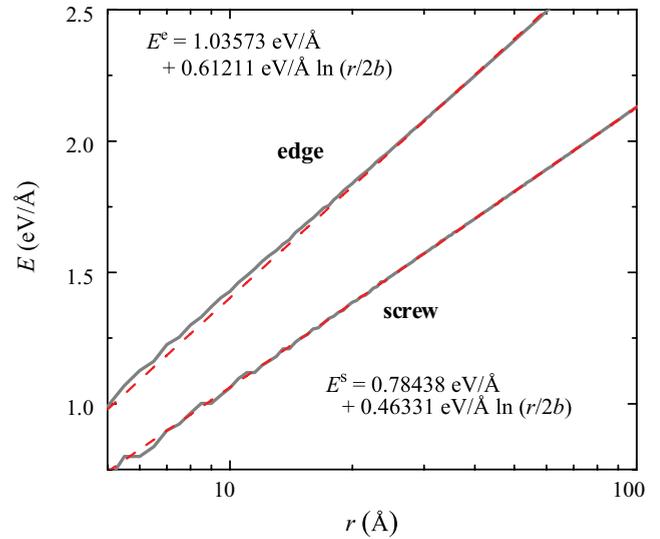
FIG. 5. (Color online) Energy of the $\langle 111\rangle/2$ screw dislocation and the $\frac{1}{2}\langle 111\rangle\{112\}$ edge dislocation as functions of radius for the MEAM potential. The fitted points for $r > 20$ Å are shown as dashed lines extrapolated to $r = 0$.

dislocation. K is the shear modulus that only depends on the elastic constants[75] and ν is Poisson's ratio.

Figure 5 shows the fit of this equation to the MEAM results for the screw and edge dislocation. There is little scatter of the energy down to the atomic scale. Using the MEAM values of the elastic constants we calculate $K = 126$ G Pa and $\nu = 0.29$. The fit to the dislocation energy yields $K = 124$ G Pa and $\nu = 0.24$. The core energy per unit length for a chosen core radius of $2b$ of the screw dislocation (0.784 eV/Å) is lower than for the edge (1.036 eV/Å).

Figure 6(a) shows the relaxed core structure of the $\langle 111\rangle/2$ screw dislocation. The core structure is symmetric with atomic displacements spread symmetrically across the $(\bar{1}01)$, $(0\bar{1}1)$, and $(\bar{1}10)$ planes. The same type of core structure of the screw dislocation of Mo is obtained by DFT methods[13,19] and tight binding.[16] The results are presented using differential displacement maps introduced by Vitek *et al.*[77] The atoms are projected into the (111) plane, and the arrows represent relative atomic displacements of neighboring atoms in the [111]. The lengths of the arrows are scaled such that an arrow connects two atoms if the difference in their displacements is $b/3$. The shadings of the atoms indicate that there are three repeating layers of atoms in the [111] direction in an ideal crystal.

Figure 6(b) shows Peierls stresses for dislocation motion for various orientations of the maximum resolved shear stress plane (MRSSP). We use χ to represent the angle between the MRSSP and the $(\bar{1}01)$ planes. We gradually increase the strain on the structure with the dislocation and allow the atoms to relax after each increase in strain. The resulting shear stress acts in the MRSSP, and the dislocation moves when the stress reaches the Peierls stress. The dislocation moves along the $(\bar{1}01)$ plane for all the MRSSP orientations of $-30 < \chi < 30°$. The results of Fig. 6(b) clearly demonstrate the dependence of the Peierls stress on the sense of shearing and illustrate the well-known breakdown of Schmid's law in bcc metals.[1–8] Schmid's law predicts slip begins when the shear

TABLE VI. Peierls stress for the $\langle 111 \rangle/2$ screw dislocation in bcc Mo. The stresses are given in units of G Pa. The experimental values are estimated by extrapolation of the low-temperature experiments of Ref. [76] to $T = 0$.

	Twinning ($\bar{1}\bar{1}2$)	($\bar{1}01$)	Antitwinning ($\bar{2}11$)
Experiment[a]	0.69	0.87	–
MEAM[b]	2.02	1.79	2.36
DFT[c]	–	1.8	–
FP-GFBC[d]	1.74	2.09	3.48
BOP[e]	2.8	2.6	3.5
MGPT[f]	2.34	2.61	7.29
MGPT[g]	–	3.44	–
Tight binding[h]	–	3.8	–
F-S[h]	–	2.4	–

[a]Experimental data.[76]
[b]This work.
[c]DFT results of Shimizu *et al.*[19]
[d]First-principles GFBC results of Woodward and Rao.[13]
[e]BOP results of Mrovec *et al.*[17]
[f]MGPT results of Rao and Woodward.[12]
[g]MGPT results of Xu and Moriarty.[10]
[h]Results of Li *et al.*[16]

of experimental samples.[8] Another possible explanation for the discrepancy is that at elevated stress the energetic barriers for kink nucleation are so reduced that a single nucleation event can trigger a series of subsequent nucleation events. Such an avalanche of kink nucleation events would lead to an increased traversal distance per nucleation event and, hence, to a lower activation energy than calculated for dislocation motion.[78]

V. CONCLUSION

We developed and tested an empirical potential that accurately describes the mechanical properties of the technologically important Mo system. The potential is of the modified embedded-atom form, ensuring computational efficiency, with parameters optimized to density-functional calculations. The predictions of the potential closely match density-functional results for structural and elastic properties, phonon frequencies, point defect formation energies, compression and thermal-expansion curves, surface energies, ideal shear strength, and gamma surfaces even when these were not included in the fitting procedure. The empirical potential captures many features of the DFT potential-energy landscape, as verified by the close agreement of the relative energies of metastable crystal structures found using a genetic algorithm structure generator. The accuracy of the potential for mechanical properties of Mo was successfully demonstrated by calculating the core structures, energies, and Peierls stresses of screw and edge dislocations.

FIG. 6. (Color online) (a) Differential displacement plots of a $\langle 111 \rangle/2$ screw dislocation in Mo and (b) Peierls stresses for dislocation motion as a function of MRSSP orientation.

stress resolved on the slip plane and slip direction exceeds the critical resolved shear stress, independent of any other stress components. Deviation from Schmid's law starts around $\chi \gtrsim 15°$ and rapidly increases as the MRSSP approaches the ($\bar{2}11$) plane.

For pure shear on the ($\bar{1}01$) plane ($\chi = 0$) the Peierls stress of our MEAM potential for the $\langle 111 \rangle/2$ screw dislocation is 1.79 G Pa. This value is an order of magnitude higher than the calculated Peierls stress value of 0.15 G Pa for the $\frac{1}{2}\langle 111 \rangle \{112\}$ edge dislocation, confirming that the plastic behavior of bcc metals is mainly controlled by screw dislocations. Table VI lists results of our MEAM potential for $\chi = -30$, 0, and 30° along with experimental data[76] and results from previous calculations. For the ($\bar{1}01$) plane the predictions of the Peierls stress vary between 1.8 and 3.8 G Pa depending on the method and simulation setup.[10,12,13,16,17,19] However, all these simulated Peierls stresses are two to four times higher than the experimental value of 0.87 G Pa. This discrepancy between experimentally measured yield stresses and the values from the atomistic simulations has been noted for most bcc metals. It has been proposed that the internal stress concentrations due to the elastic interaction among a large number of dislocations on the mesoscopic scale may be the origin of the lower yield stresses

---

*Corresponding author: hkpark@mps.ohio-state.edu.

[1]L. P. Kubin, Rev. Deform. Behav. Mater. **4**, 181 (1982).

[2]J. W. Christian, Metall. Trans. A **14**, 1237 (1983).

[3]M. S. Duesbery, in *Dislocations in Solids*, edited by F. R. N. Nabarro, Vol. 8 (Elsevier, Amsterdam, 1989), pp. 66–173.

[4]V. Vitek, Prog. Mater. Sci. **36**, 1 (1992).

[5]A. Seeger, J. Phys. IV **5**, 45 (1995).

[6]W. Pichl, Phys. Stat. Sol. A **189**, 5 (2002).

[7]M. S. Duesbery, V. Vitek, and J. Cserti, in *Understanding Materials,* edited by C. J. Humphreys (Maney, London, 2002), pp. 165–192.

[8]R. Gröger and V. Vitek, Phil. Mag. Lett. **87**, 113 (2007).

[9]W. Xu and J. A. Moriarty, Phys. Rev. B **54**, 6941 (1996).

[10]W. Xu and J. A. Moriarty, Comput. Mater. Sci. **9**, 348 (1998).

[11]S. Ismail-Beigi and T. A. Arias, Phys. Rev. Lett. **84**, 1499 (2000).

[12]S. I. Rao and C. Woodward, Phil. Mag. A **81**, 1317 (2001).

[13]C. Woodward and S. I. Rao, Phil. Mag. A **81**, 1305 (2001).

[14]C. Woodward and S. I. Rao, Phys. Rev. Lett. **88**, 216402 (2002).

[15]Y. Li, D. J. Siegel, J. B. Adams, and X.-Y. Liu, Phys. Rev. B **67**, 125101 (2003).

[16]J. Li, C.-Z. Wang, J.-P. Chang, W. Cai, V. V. Bulatov, K.-M. Ho, and S. Yip, Phys. Rev. B **70**, 104113 (2004).

[17]M. Mrovec, D. Nguyen-Manh, D. G. Pettifor, and V. Vitek, Phys. Rev. B **69**, 094115 (2004).

[18]D. R. Trinkle and C. Woodward, Science **310**, 1665 (2005).

[19]F. Shimizu, S. Ogata, H. Kimizuka, T. Kano, J. Li, and H. Kaburaki, J. Earth Simulator **7**, 17 (2007).

[20]M. I. Baskes, Phys. Rev. Lett. **59**, 2666 (1987).

[21]T. J. Lenosky, B. Sadigh, E. Alonso, V. V. Bulatov, T. D. de la Rubia, J. Kim, A. F. Voter, and J. D. Kress, Modelling Simul. Mater. Sci. Eng. **8**, 825 (2000).

[22]R. G. Hennig, T. J. Lenosky, D. R. Trinkle, S. P. Rudin, and J. W. Wilkins, Phys. Rev. B **78**, 054121 (2008).

[23]G. Kresse and J. Hafner, Phys. Rev. B **47**, R558 (1993).

[24]G. Kresse and J. Furthmüller, Phys. Rev. B **54**, 11169 (1996).

[25]P. E. Blochl, Phys. Rev. B **50**, 17953 (1994).

[26]G. Kresse and D. Joubert, Phys. Rev. B **59**, 1758 (1999).

[27]J. P. Perdew, K. Burke, and M. Ernzerhof, Phys. Rev. Lett. **77**, 3865 (1996).

[28]J. G. Swadener, M. I. Baskes, and M. Nastasi, Phys. Rev. Lett. **89**, 085503 (2002).

[29]M. I. Baskes, J. S. Nelson, and A. F. Wright, Phys. Rev. B **40**, 6085 (1989).

[30]B.-J. Lee and M. I. Baskes, Phys. Rev. B **62**, 8564 (2000).

[31]B.-J. Lee, J.-H. Shim, and M. I. Baskes, Phys. Rev. B **68**, 144112 (2003).

[32]Y.-M. Kim, B.-J. Lee, and M. I. Baskes, Phys. Rev. B **74**, 014101 (2006).

[33]M. I. Baskes, Phys. Rev. B **46**, 2727 (1992).

[34]S. Birner, J. Kim, D. A. Richie, J. W. Wilkins, A. F. Voter, and T. Lenosky, Solid State Commun. **120**, 279 (2001).

[35]C. V. Ciobanu and C. Predescu, Phys. Rev. B **70**, 085321 (2004).

[36]Y. A. Du, R. G. Hennig, T. J. Lenosky, and J. W. Wilkins, Eur. Phys. J. B **57**, 229 (2007).

[37]H. Park and J. W. Wilkins, Phys. Rev. B **79**, 241203 (2009).

[38]S. A. Ghasemi, M. Amsler, R. G. Hennig, S. Roy, S. Goedecker, T. J. Lenosky, C. J. Umrigar, L. Genovese, T. Morishita, and K. Nishio, Phys. Rev. B **81**, 214107 (2010).

[39]H. Park and J. W. Wilkins, Appl. Phys. Lett. **98**, 171915 (2011).

[40]Y. A. Du, T. J. Lenosky, R. G. Hennig, S. Goedecker, and J. W. Wilkins, Phys. Status Solidi B **248**, 2050 (2011).

[41]S. Goedecker, Comput. Phys. Communications **148**, 124 (2002).

[42]J. Kim, *Ohmms*, https://sites.google.com/a/cmscc.org/ohmms/ (2004).

[43]F. Stillinger and T. Weber, Phys. Rev. B **31**, 5262 (1985).

[44]W. H. Press, S. A. Teukolsky, W. T. Vetterling, and B. P. Flannery, *Numerical Recipes in C*, 2nd ed. (Cambridge University Press, New York, 1993).

[45]M. J. D. Powell, Comput. J. **7**, 303 (1965).

[46]R. H. Swendsen and J.-S. Wang, Phys. Rev. Lett. **57**, 2607 (1986).

[47]C. J. Geyer, in *Computing Science and Statistics: Proceedings of the 23rd Symposium on the Interface* (American Statistical Association, New York, 1991), p. 156.

[48]E. Marinari and G. Parisi, Europhys. Lett. **19**, 451 (1992).

[49]L. Brewer, Lawrence Berkeley Laboratory Report No. LBL-3720, 1977.

[50]W. B. Pearson, *Handbook of Lattice Spacing and Structures of Metals* (Pergamon, Oxford, 1967), Vol. 2.

[51]G. Simmons and H. Wang, *Single Crystal Elastic Constants and Calculated Aggregate Properties: A Handbook*, 2nd ed. (MIT Press, Cambridge, 1971).

[52]S. J. Plimpton, J. Comp. Phys. **117**, 1 (1995); more information about LAMMPS is found at http://lammps.sandia.gov.

[53]C. Kittel, *Introduction to Solid State Physics, 7th ed.* (Wiley, New York, 1996).

[54]F. Birch, J. Geophys. Res. **83**, 1257 (1978).

[55]M. J. Mehl, B. M. Klein, and D. A. Papaconstantopoulos, in *Intermetallic Compounds: Principles and Practice, Volume I: Principles,* edited by J. H. Westbrook and R. L. Fleischer (Wiley, London, 1995), pp. 195–210.

[56]W. W. Tipton and R. G. Hennig, *Gasp*, http://gasp.mse.cornell.edu/ (2011).

[57]W. Bi, Y. Meng, R. S. Kumar, A. L. Cornelius, W. W. Tipton, R. G. Hennig, Y. Zhang, C. Chen, and J. S. Schilling, Phys. Rev. B **83**, 104106 (2011).

[58]D. Nguyen-Manh, A. P. Horsfield, and S. L. Dudarev, Phys. Rev. B **73**, 020101 (2006).

[59]S. Han, L. A. Zepeda-Ruiz, G. J. Ackland, R. Car, and D. J. Srolovitz, Phys. Rev. B **66**, 220101R (2002).

[60]J. M. Harder and D. J. Bacon, Philos. Mag. A **54**, 651 (1986).

[61]T. R. Mattsson and A. E. Mattsson, Phys. Rev. B **66**, 214110 (2002).

[62]B. M. Powell, P. Martel, and A. D. B. Woods, Phys. Rev. **171**, 727 (1968).

[63]R. Kinslow, *High-Velocity Impact Phenomena* (Academic Press, New York, 1970).

[64]Y. S. Touloukian, R. K. Kirby, R. E. Taylor, and P. D. Desai, *Thermophysical Properties of Matter: Thermal Expansion—Metallic Elements and Alloys* (Plenum Press, New York, 1975), Vol. 12.

[65]D. Alfè, Comput. Phys. Commun. **180**, 2622 (2009).

[66]L. Z. Mezey and J. Giber, Jpn. J. Appl. Phys. **21**, 1569 (1982).

[67]B.-J. Lee, M. Baskes, H. Kim, and Y. Koo Cho, Phys. Rev. B **64**, 184102 (2001).

[68]A. B. Belonoshko, R. Ahuja, and B. Johansson, Phys. Rev. Lett. **84**, 3638 (2000).

[69]M. R. Fellinger, H. Park, and J. W. Wilkins, Phys. Rev. B **81**, 144119 (2010).

[70]D. Errandonea, B. Schwager, R. Ditz, C. Gessmann, R. Boehler, and M. Ross, Phys. Rev. B **63**, 132104 (2001).

[71]M. L. Hildner, R. S. Daley, T. E. Felter, and P. J. Estrup, J. Vac. Sci. Technol. A **9**, 1604 (1991).

[72]A. J. Melmed, S. T. Ceyer, R. T. Tung, and W. R. Graham, Surf. Sci. **111**, L701 (1981).

[73]A. Paxton, P. Gumbsch, and M. Methfessel, Philos. Mag. Lett. **63**, 267 (1991).

[74]V. Vitek, Phil. Mag. **18**, 773 (1968).

[75]A. K. Head, Phys. Stat. Sol. **6**, 461 (1964).

[76]L. Hollang, D. Brunner, and A. Seeger, Mater. Sci. Eng. A **319-321**, 233 (2001).

[77]V. Vitek, R. C. Perrin, and D. K. Bowen, Phil. Mag. **21**, 1049 (1970).

[78]T. Suzuki and H. Koizumi, Phil. Mag. A **67**, 1153 (1993).